Noncontact Mutual-Inductance-Based Measurement of an Inhomogeneous Topological Insulating State in Bi_2Se_3 Single Crystals with Defects

Amit Jash,[1] Kamalika Nath,[1] T.R. Devidas,[2,†] A. Bharathi,[2] and S.S. Banerjee[1,*]

[1]*Department of Physics, Indian Institute of Technology, Kanpur 208016, Uttar Pradesh, India*
[2]*UGC-DAE Consortium for Scientific Research, Kalpakkam 603104, India*

Pure topological insulating materials preserve a unique electronic state comprised of a bulk insulating gap and conducting surface states. We use bulk Bi_2Se_3 single crystals possessing Se vacancy defects as a prototype topological insulator (TI) material for exploring the effect of nonmagnetic disorder on the conducting properties of TIs. We employ a sensitive, noncontact mutual-inductance-based technique for measuring the surface and bulk contributions to electrical conductivity in the TI. We discern the bulk and surface contributions by observing that the predominant surface electrical conduction shows a linear frequency dependence of the pickup signal while bulk conductivity gives rise to a quadratic frequency dependence. We also observe an algebraic temperature-dependent surface conductivity and an activated form of bulk electrical conductivity. Using the above, we uncover an interplay between surface and bulk contributions to electrical conductivity in the TI as a function of temperature. In the Bi_2Se_3 crystals, the transformation from surface to bulk-dominated electrical transport is found to occur close to a temperature of 70 K. This temperature matches well with our results from activated bulk electrical transport results, which show an activation energy scale Δ, which is in the meV range. The gap Δ is much less than the bulk band gap in Bi_2Se_3, which we argue is associated with defect states in the TI material. To understand our results, we propose a model of TI comprised of an inhomogeneous low electrically conducting medium (bulk), which is sandwiched between two thin high electrically conducting sheets (surface). We argue that the inhomogeneous TI state is generated by selenium vacancy defects in Bi_2Se_3, which are responsible for producing an interplay between bulk and surface conductivities.

I. INTRODUCTION

In recent times, new materials such as three-dimensional (3D) topological insulators, exhibit a topologically protected bulk gapped state enclosed by a conducting surface state [1–6]. Herein, no continuous variation of the lattice parameter can change the unique character of the electronic states in these materials. These gapless surface states in a topological insulator (TI) exhibit Dirac-like linear energy-momentum dispersion [7,8], chiral spin texture [5], and Landau level quantization [9]. Materials such as Bi_2Se_3, Bi_2Te_3, and $Bi_{1-x}Sb_x$ are among the most well studied three-dimensional TIs [2,7,10]. The characteristic TI properties have been confirmed via different techniques such as angle-resolved photoemission spectroscopy (ARPES) [3,5,11,12], Shubnikov-de Haas (SdH) oscillations, [13,14] STM, and transport studies [2,15]. Spin momentum locking in a TI causes chiral currents to flow, which are unaffected by scattering from disorder

[1,2,15,16]. Recent developments of pump probe techniques to study spin momentum locking [17] reveal that TIs are important from the point of view of spintronics and quantum computation applications [18–20]. While pristine TIs are important, it is also important to explore how the TI state is affected in the presence of material defects. While the presence of magnetic impurities will lead to breaking time reversal symmetry and hence destroy the TI state, the issue of how nonmagnetic disorder affects the TI state is worth investigating.

To study the effect of disorder on TI, the popular Bi_2Se_3 crystals are a suitable choice as they intrinsically possess Se vacancies, which are a natural source of disorder in this material. The TI nature of Bi_2Se_3 has been identified through magnetotransport studies, which confirm the presence of conducting surface states through the observation of SdH oscillations and weak antilocalization effects [16,21–25]. In Bi_2Se_3, the bulk insulating gap has been estimated to be approximately 300 meV [7,10,26,27]. However, the presence of Se vacancy electrons dopes the material [28–30], thereby enhancing the bulk electrical conductivity. The resulting parallel conducting channels through the surface and bulk make it difficult to explore

_____

*satyajit@iitk.ac.in
†Present address: The Racah Institute of Physics, Hebrew University of Jerusalem, Givat Ram, Jerusalem, 91904, Israel.

the details of the individual bulk and surface state contributions to electrical conductivity in these TI materials [6,31,32]. In such materials, the surface states have been identified either by suppressing the defect-induced bulk conductivity through counter doping [7,15] or by comparing changes in the conducting properties as a function of the thickness of TI thin films [21–23,33,34]. Without counter doping, the issue of investigating how Se vacancies affect the TI state in Bi_2Se_3 single crystals is none the less important. Studies show that increasing the Se vacancy concentration weakens the SdH oscillations, which is a fingerprint of the conducting surface states characterizing a TI [21–24,33–36]. The SdH oscillations in magnetotransport are typically measurable at a low temperature and high magnetic field regime. Hence, due to the limitations of the transport studies mentioned above, while the presence of disorder such as Se vacancies seem to weaken the TI state, the details of exactly how the surface and bulk conductivities are affected by disorder and modified by Se vacancies still remain unclear. Furthermore, studies have shown that degradation of the surface of Bi_2Se_3, for example, due to oxidation of the surfaces, causes band bending of the surface states extending up to 20 nm into the bulk [37,38]. Hence, there is a need for a technique that distinguishes between bulk and surface contributions to electrical conductivity in a TI. We report here a noncontact measurement technique of shielding currents induced in a TI using a two-coil mutual-inductance setup. We study the frequency (f) and temperature (T) dependence of the pickup voltage from five single crystals of different thicknesses of Bi_2Se_3 placed between the coils. The pickup voltage shows two distinct regimes of frequency dependence (viz., quadratic and linear regimes). We show that the quadratic frequency dependence is associated with bulk electrical conductivity in the TI while the linear frequency dependence regime is associated with surface conductivity in the TI. As a function of temperature, we show that below 70 K, the frequency dependence of the pickup voltage is predominantly linear while it becomes quadratic at higher T. Analysis of the data also shows that below 70 K, we identify an algebraic temperature-dependent electrical conductivity regime that saturates at low temperatures, while above 70 K, electrical conductivity is of a thermally activated type with a thermal activation energy scale (Δ) of tens of meV. From our study, we identify four distinct temperature regimes for the Bi_2Se_3 crystal, identifying the crossover between different surface- and bulk-dominated conductivity regimes. At high temperatures above 180 K, we observe the unusual return of surface-dominated conductivity (σ_s) coexisting with bulk conductivity (σ_b) in the material. To understand our results, we propose a simplified model of a TI, comprised of a low-conducting bulk sandwiched between two high-conducting surface sheets. Our simulations show surface and bulk conductivity values in the Bi_2Se_3 crystals to be of the order of 10^{11} S/m and

10^3 S/m, respectively. While this minimal model explains the overall features of the data and offers a way to estimate the surface and bulk electrical conductivities of the TI from the measurements, it does not match the data exactly. A better agreement with the data is obtained by considering an inhomogeneous TI state. Inhomogeneous TI is modeled by incorporating in the minimal model conducting channels threading the low-conducting bulk medium. The model fits our experimental data by introducing an inhomogeneity of 30%. The inhomogeneous TI state we argue is a result of disorder in the TI bulk, generated by selenium vacancies. Excess charge carriers produced by Se vacancies produce the gap of approximately Δ, which results in an interplay between bulk and surface conductivities.

II. EXPERIMENTAL DETAILS: TRANSPORT MEASUREMENT OF Bi_2Se_3 SINGLE CRYSTALS

For our study, we use single crystals of Bi_2Se_3 prepared by slow cooling stoichiometric melts of high-purity bismuth (Bi) and selenium (Se) powders [for details see Refs. [35,36]]. In this work, we have investigated the surface and bulk conductivities across five different single crystals belonging to the same batch of Bi_2Se_3 crystals grown (with similar electrical transport characteristics, for example, see Fig. 1). The thicknesses (surface areas) of the crystals are, 20 μm (2.4 $\times$ 1.9 mm^2) (hence forth referred to as the $S20$ sample), 51 μm ($S51$) (2.8 $\times$ 2.5 mm^2), 69 μm ($S69$) (3.9 $\times$ 2.5 mm^2), 75 μm ($S75$) (3.7 $\times$ 2.6 mm^2), and 82 μm ($S82$) (3.2 $\times$ 2.8 mm^2). The electrical transport measurements shown in Fig. 1 are on a Bi_2Se_3 single crystal with a thickness of 70 μm. Note that as transport measurements involve the making of electrical contacts on the sample, which introduce irreversible physical changes in the sample, hence for our noncontact measurements (which is the main topic of our manuscript) and transport measurements (here and Refs. [35,36]), we are compelled to use different samples for the two measurements, albeit chosen from the same batch of single crystals grown with similar sample thicknesses. Figure 1(a) shows distinct SdH oscillation in longitudinal magnetoresistance [R_{xx} vs magnetic field (B)] measurements at different temperatures using standard Van der Pauw geometry. The low-temperature SdH oscillations, which weaken with increasing T, indicate the topological character of conducting surface states in TI at low T [13,14,21–23,35,36] (more detailed analysis of the transport data is shown elsewhere [35,36]). The figure shows that the topological character of transport is progressively affected with increasing T. The Berry phase (ϕ) is calculated from the Lifshitz-Kosevich (LK) fitting and the value is close to π at low T, which suggests the SdH oscillation arises from a surface Dirac electron [see inset of Fig. 1(b) and is discussed in a later section]. The destruction of the SdH oscillations is
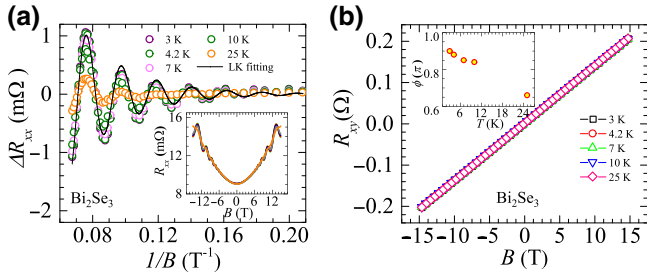
FIG. 1. (a) Inset shows the variation of R_{xx} as a function of magnetic field B measured in the standard Van der Pauw geometry at 3 K, 4.2 K, 7 K, 10 K, and 25 K (see legends in the main panel). The main panel shows ΔR_{xx} vs $1/B$ plot showing SdH oscillations in Bi_2Se_3 (sample thickness 70 μm) at different temperatures. ΔR_{xx} is calculated by subtracting from the experimental $R_{xx}(B)$ values a polynomial fit to the data (R_{poly} (B)), where B is the magnetic field. The data is fitted to $R_{poly}(B) = R_0 + R_1B + R_2B^2$, where $R_0 = 9.26 \times 10^{-3}$ Ω, $R_1 = -1.71 \times 10^{-6}$ Ω T^{-1}, $R_2 = 2.91 \times 10^{-5}$ Ω T^{-2}. The LK equation is used to fit the ΔR_{xx} data at 4.2 K, which is shown by the black solid line. For fitting to the magnetoresistance data in Fig. 1(a), following Ref. [35] and the values therein, we use $\Delta R_{xx} = a\sqrt{0.011B}[(11.12/B)/\sinh(11.12/B)]e^{-(19.38/B)}(0.95)\cos[2\pi\{(F/B) + \beta\}]$. In this equation, $a = 0.0135$ Ω and F and β are the fitting parameters. A fit to the data [see black solid line in Fig. 1(a)] gives $F = 46.95 \pm 0.25$ T and $\beta = 0.43$. (b) Hall measurement of the transverse resistance R_{xy} vs B at different temperatures. The sample used in the above measurements has a thickness of approximately 70 μm. Inset shows the Berry phase as a function of temperature, which is measured from the phase of the LK equation (viz., $\phi = 2\pi\beta$).

identified with the onset of bulk contribution to the electrical conductivity. Figure 1(b) shows the Hall resistance (R_{xy}) measurement as a function of magnetic field (B) at different temperatures. This measurement establishes electrons as the charge carriers in these Bi_2Se_3 samples. It may be recalled that electrical transport measurement studies have shown that Se vacancies lead to weakening the SdH oscillations [35,36]. Recent studies show a correlation between positron annihilation lifetime with Se vacancy concentration in Bi_2Se_3. These studies, performed on this batch of samples, show Se vacancy concentrations are in the range of 10^{17} cm^{-3} [35]. From these SdH measurements at low T and high B, it is, however, difficult to determine the extent of surface and bulk contributions to conductivity, and hence study how it is affected by either T or disorder variation present either on the surface or bulk of the material (note, we shall return to this issue in the discussion section). As mentioned earlier, the appearance of finite bulk conductivity in the Bi_2Se_3 sample with Se vacancies mixes the surface and bulk contributions to electrical conductivity making it difficult to discern the individual contributions. In the next section, we discuss a noncontact measurement technique, which allows us

to distinguish between the two contributions to electrical conductivity.

III. TWO-COIL MUTUAL-INDUCTANCE MEASUREMENT SETUP: NONCONTACT MEASUREMENT

To characterize the surface and bulk states of TI, we use a modified noncontact two-coil mutual-inductance measurement technique. The two-coil mutual-inductance technique is well-established experimentally [39–42] and it is sensitive enough to experimentally study the shielding response of superconductors, especially in situations when it becomes weak such as that near the critical temperature of a superconductor. The technique has been analyzed theoretically to determine the nature of the field and current distributions generated in the sample placed within the two-coil configuration by incorporating the effects of skin depth or penetration depth [43–45] and studying the behavior of the pickup signal generated. Note that whereas in conventional electrical transport measurement the Joule heating at electrical contacts complicates temperature-dependent conductivity measurements, here, such issues are avoided through our noncontact two-coil mutual-inductance measurement technique. Figure 2(a) shows the schematic of our setup where a crystal is placed between an excitation coil and a pickup coil. Both coils are designed with very closely matched coil parameters (for details on coil dimensions and other parameters see S1 within the Supplemental Material [46]). The data for all our pickup measurements corresponds to an ac current of amplitude 153 mA applied to the excitation coil (corresponding to a volt drop across the coil) at frequency f, and the real and imaginary components of the pickup voltage from the pickup coil are measured using a lock-in amplifier. Measurements at higher ac excitation current amplitudes yield similar results. In S1 within the Supplemental Material (Ref. [46]), we show the linear relationship between the excitation current in the coil and the pickup voltage for an $S20$ sample at 65 kHz excitation frequency. The excitation current generates a time-varying magnetic field, which induces currents inside the conducting sample that in turn lead to a time-varying magnetic field associated with the sample. This local field induces a voltage in the pickup coil that is being measured. Effectively, one considers that the presence of a sample between the two coils modifies the mutual inductance. Variations in the sample properties change the signal induced in the pickup coil. One may note that voltage is induced in the pickup coil not only from time-varying magnetic fields associated with the sample, but also via the stray magnetic fields present outside the sample. These stray field-induced pickup voltage signals can often lead to a large background signal, which masks the signal from the sample if it is weak. In order to significantly reduce this stray field effect between the dipolar coil
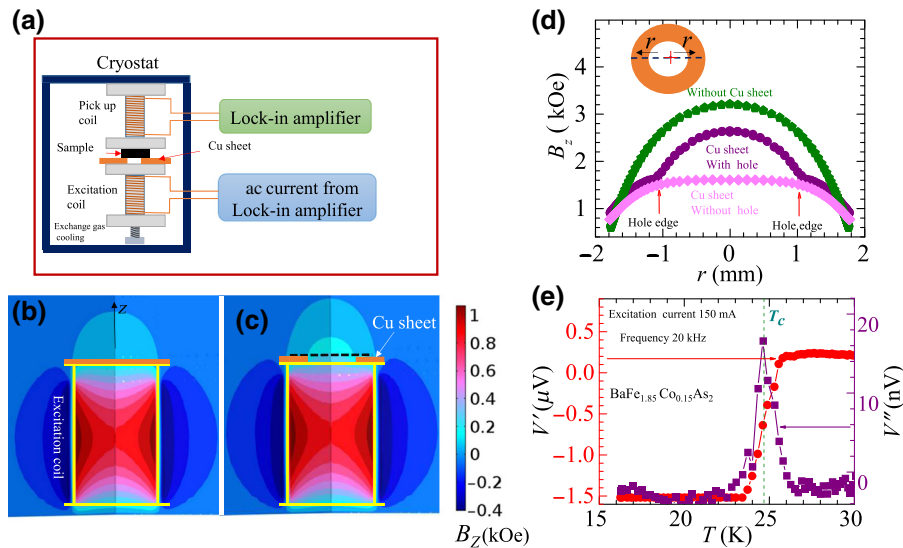
FIG. 2. (a) Schematic diagram of the two-coil mutual-inductance setup is shown. (b),(c) Show the simulated normal component of the ac magnetic field (B_Z) distribution for the two cases. The outline of the solid excitation coil bobbin is shown in yellow. In (b), only a solid Cu sheet (orange) is placed above the excitation coil and in (c), a Cu sheet with a hole at the center is placed over the coil. The sample is placed above the hole in the Cu sheet. These simulations are performed using COMSOL with a 150 mA ac current at 60 kHz sent through the excitation coil. (d) Shows the simulated B_z vs r profile as measured across the black dashed line shown in (c) ($r = 0$ is the central (z) axis of the excitation coil bobbin), for three different cases: (i) without any Cu sheet above the pickup coil, (ii) Cu sheet with a hole, (iii) Cu sheet with no hole. The inset of (d) shows the schematic of the circular Cu sheet with a hole placed over the top of the excitation coil. (e) The superconducting transition of iron pnictide single crystal, $BaFe_{1.85}Co_{0.15}As_2$, is shown. The figure depicts the behavior of the real (left axis) and imaginary (right axis) components of the pickup voltage as a function of temperature. The $BaFe_{1.85}Co_{0.15}As_2$ crystal dimension is $3.2 \times 2.4 \times 0.5$ mm^3. The T_c which is approximately 24.7 ± 0.2 K, is indicated with the green dash line. A similar T_c value of this sample is observed through bulk magnetization measurement on a superconducting quantum interference device (SQUID) magnetometer.

assembly, a 1.5-mm thick oxygen-free high-thermal conductivity Cu (OFHC) sheet (resistivity of approximately 1.7×10^{-8} Ω m) with a hole at its center [see Fig. 2(a)], is placed coaxially above the excitation coil. The hole diameter (2 mm) is chosen such that it does not exceed the sample surface dimensions (the sample is placed above the Cu sheet covering the hole). Note that the OFHC Cu sheet thickness (1.5 mm) is larger than its skin depth, which at 60 kHz is 0.27 mm and at 5 kHz is 0.92 mm. The high-conductivity thick OFHC Cu sheet shields the alternating magnetic field generated by the excitation coil, except over the hole. The electromagnetic shielding provided by the thick Cu sheet helps to reduce the stray flux linkage outside the sample, while the hole in the sheet concentrates the magnetic flux on the sample. Therefore, the Cu sheet with the hole effectively enhances the coupling of the two coils via the sample in between and the effects of the stray field are minimized. In Figs. 2(b) and 2(c), the colored regions represent the simulated vertical (z) component of the ac magnetic field distribution (B_z) around the excitation coil (for simulation details, see S2 within the Supplemental Material [46]). Figure 2(c) shows the concentration of magnetic flux above the hole in the Cu plate. In Fig. 2(d), the simulated B_z profile measured above the coil [black

dashed line in Fig. 2(c)] shows the significant concentration of magnetic flux above the hole in the Cu sheet. The sample, when placed above the Cu sheet, experiences this concentrated oscillating magnetic field and the oscillating magnetic field induces a voltage in the pickup coil voltage. Figure 2(c) shows that due to the hole in the copper sheet, the central field (amplitude of the ac field) within the coil above the hole is increased by almost a factor of two compared to the field above the solid Cu sheet outside the hole. We thus achieve almost a two times increase in the signal induced within the pickup coil due to the use of the thick copper sheet with a hole. When the sample, which is slightly larger than the hole diameter, is placed over the hole in the Cu sheet, then due to the enhancement in the field over the hole, a stronger signal emanates preferentially from the sample, which induces a voltage in the pickup coil. Thus, by using the hole in the Cu sheet, we obtain a signal that is preferentially emanating from the sample. Without the use of a Cu sheet with hole (viz., without any Cu sheet), the Fig. 2(d) (see green curve) shows the field is uniformly strong over within the entire coil area. In this configuration, if a sample is placed between the coil and the magnetic susceptibility of the sample is not high, then the signal induced in the coil will get buried in the

background signal. Here, the background signal emanates from the time varying magnetic flux in regions outside the sample area, which induces voltage in the pickup coil apart from the signal induced by the sample. Hence, the use of the Cu sheet with the hole concentrates the magnetic flux over the sample area, which, therefore, helps to induce a stronger signal in the pickup coil emanating from the sample. The use of the Cu sheet also helps to significantly reduce the stray field coupling from outside the coil area as the thick Cu sheet electromagnetically shields the alternating ac magnetic field and thereby further reduces the background signal outside the sample. This modification enhances the sensitivity of the two-coil configuration in measuring the magnetic response of the sample compared to the conventional configuration without the copper sheet with the hole. During the measurements with TI, we balance out the imaginary part of the signal as it does not change significantly during measurements. Furthermore, we would like to emphasize that for all our measurements, we subtract the background voltage at all temperatures and frequencies by measuring the pickup signal without a sample and with only the Cu sheet with a hole placed between the coils.

We test the performance of the setup using a superconducting sample as its shielding response is well known. Figure 2(e) illustrates the performance of our setup by measuring the ac susceptibility response of a superconducting single crystal, viz., an optimally doped iron pnictide crystal (BaFe$_{1.85}$Co$_{0.15}$As$_2$), which is placed above the hole in the Cu sheet. Due to the strong superconducting diamagnetic shielding of the ac magnetic field, [Fig. 2(e)], we see the rapid drop in the in-phase signal in the pickup coil (V') at $T < T_c$. Near T_c, we also see the expected peak in the out-of-phase signal (V''). To identify the negative signal below the transition temperature, we

subtract the data from the saturation value above T_c. The superconducting transition temperature T_c estimated from the peak position in V'' is 24.7 K, which compares well with the T_c reported for this stoichiometry [47,48]. The observation in Fig. 2(e) is that at the characteristic temperature T_c, there is a sharp change in the background-corrected V' signal (viz., the diamagnetic shielding response) and V'' signal (viz., the dissipation response), which suggests that these features cannot be related to features associated with the background signal (when no sample is present and only the Cu sheet with the hole is present). The behavior of the background signal of the two-coil setup (with only the Cu sheet placed between the hole) is simulated and the pickup voltage signal due to the solid Cu sheet is shown in the Supplemental Material (see S3 within the Supplemental Material [46]). The close match between the experimentally measured background signal with the simulated data (S3 within the Supplemental Material [46]) shows that the background signal can be explained using standard Maxwell's equations for a metallic conductor. There is nothing in the equations that can cause a nonmonotonic change in the background signal.

IV. STUDYING THE SHIELDING RESPONSE OF A Bi$_2$Se$_3$ SINGLE CRYSTAL AT DIFFERENT f AND T

Figure 3(a) shows the $V(f)$ measured for the $S69$ Bi$_2$Se$_3$ sample at different temperatures, where $V(f) = \sqrt{V'^2(f) + V''^2(f)} \approx V'(f)$, as for these TI crystals, $V''(f) \ll V'(f)$. In the figure, one can identify two regimes of behavior in $V(f)$, namely, one in the low-frequency regime where $V(f) \propto f^2$ (see red dotted line through the data), and the other in the higher frequency regime where $V(f) \propto f^\alpha$ (where $\alpha = 0.9 \pm 0.05$) (see black solid line
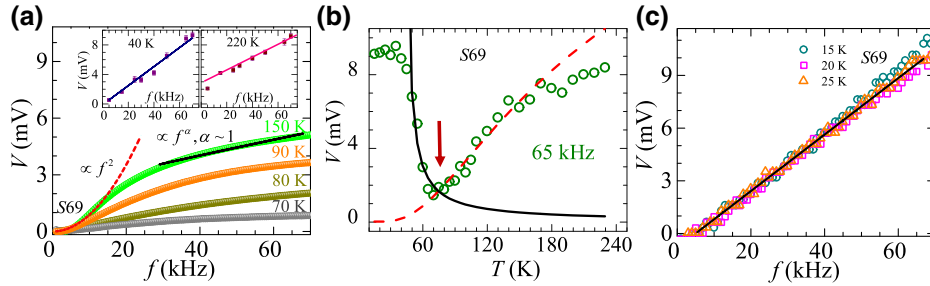

FIG. 3. (a) Shows $V(f)$ responses at higher temperatures, 150 K, 90 K, 80 K, and 70 K (from top to bottom curves). The quadratic ($V(f) \propto f^2$) and nearly linear ($V(f) \propto f^\alpha$, where $\alpha = 0.9 \pm 0.05$) regions are shown by the dotted red line and solid black line, respectively. Insets show pickup response at 40 K and 220 K (V is measured from $V(T)$ scan at different frequencies). For both 40 K and 220 K above 20 kHz, V is increasing linearly with frequency. All data in the figures correspond to an excitation current of 153 mA in the excitation coil. (b) Variation of pickup voltage (V) with temperature (T) for sample $S69$ at frequency 65 kHz. Red dotted line is the fitted line corresponding to bulk conductivity [viz., $V \propto V_{b0} \exp(-\Delta/K_b T)$] and the black line is fitted with surface conductivity, that is, $V \propto (1/(C' + D'T)$. The fitting parameters are $C' = 0.0052$ mV^{-1}, $D' = 1.86$ mV^{-1} K^{-1}, $V_{b0} = 18.7$ mV, and Δ is (25.2 ± 1.25) meV. (c) The behavior of the pickup voltage with frequency is plotted at different low temperatures (15 K, 20 K, and 25 K).

to the data). The $V(T)$ data in Fig. 3(b) shows that the pickup voltage saturates to a constant value at a low T up to 40 K. Above 40 K to 70 K, the $V(T)$ data fits (solid black line) with $\sigma_s(T) = 1/(C + DT)$ where C is related to static disorder scattering and D to electron-phonon coupling strength. While above 70 K to 170 K, the data fits (red dashed line) with $\sigma_b(T) = \sigma_{b0}\exp(-\Delta/K_bT)$, $\Delta \sim 25.2 \pm 1.25$ meV, where Δ is the activation energy scale and σ_{b0} is the high-temperature conductance of the bulk state. Above the temperature of 170 K, the data deviates from the thermally activated behavior, which is present between 70 K and 170 K. Figure 3(c) shows that $V(f)$ is linear over a wide frequency regime at $T \leq 40$ K. The inset of Fig. 3(a) shows that at 40 K, $V(f)$ increases linearly with f for the entire frequency range. At 220 K [see Fig. 3(a) inset], $V(f)$ is not quadratic but $V(f) \propto f^{\alpha}$ above 20 kHz, where $\alpha \sim 1$ (viz., almost linearly dependent). Between 70 K and 170 K, $V(f) \propto f^2$ for $f \leq 20$ kHz and $V(f) \propto f^{\alpha}$, where $\alpha \sim 1$ for higher frequencies. Identical features at different f and T are shown in the Supplemental Material [46] for other samples as well (see S4, S5, S6, S7, and S8 within the Supplemental Material [46]).

We would like to mention that the pickup signal at low f is less than that at 70 kHz in a frequency-dependent measurement or it is less at low T compared to that above 300 K in a T-dependent measurement. Therefore, while measuring the pickup signal as a function of f or T, one can balance out the signal above 70 kHz or 300 K to note the negative sign of the pickup signal corresponding to the diamagnetic nature of Bi_2Se_3.

V. UNDERSTANDING THE FREQUENCY DEPENDENCE OF THE PICKUP SIGNAL

To understand the above frequency dependence of the pickup voltage, we recall that the ac magnetic field produced from the excitation current in the primary induces screening currents extending up to different depths inside the conducting TI sample (skin depth). The magnetic field generated from the sample by these induced screening currents couples with the pickup coils to induce a pickup voltage. It is known that the depth up to which the currents are induced in the sample depends on the frequency of the ac field. At low frequencies, as the ac excitation penetrates deeper into the bulk of the sample (due to large skin depth), the bulk properties in the TI sample are probed with a low f. The schematic of the distribution of the magnitude of the induced screening current ($I_{induced}$) across the sample cross section is shown in Figs. 4(a) and 4(b) for low frequency and high frequency, respectively. The expression for skin depth (δ) is $\sqrt{1/\pi\sigma f\,\mu}$, where μ is the permeability of Bi_2Se_3. At high frequency Fig. 4(b), screening currents circulate within the high-conductivity surfaces. We show in S11 within the Supplemental Material [46], a simulation showing the attenuation of an impinging em signal is governed by the high-conducting surface sheath in the TI material. Hence, the properties of the surface state of the TI is probed at high f. At low frequency [Fig. 4(a)], the induced current circulates in the bulk of the sample. In Fig. 4(c), we plot the pickup voltage versus the sample surface area for all five samples having varied thicknesses. Note that above 120 K at 5 kHz as the current induces in the bulk of the sample, the pickup signal saturates to a value close to 1 mV for all samples, which shows no scaling with surface area. In fact, at high frequency and low T (65 kHz and 25 K) as the highly conducting surface states are effectively probed, the pickup voltage scales with the sample surface area. At low T, numerous studies [13,14,21,22] as well as the SdH oscillation in Fig. 1(a) confirm the dominance of surface conductivity in the TI. In this regime, the observation of $V(f) \propto f^{\alpha}$, where $\alpha \sim 1$, suggests the linear frequency dependence of pickup voltage $V(f)$ is related to the contribution to electrical conduction from the surface state of the TI. The emergence of the $V(f) \propto f^2$ at low
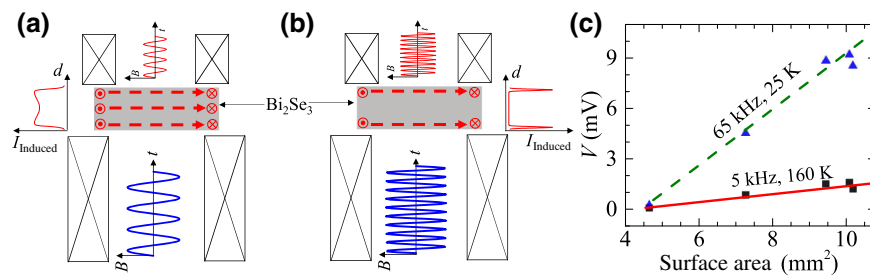

FIG. 4. (a) Shows the schematic of the magnitude of the induced current distribution across the sample cross section at a lower frequency. The induced current is shown to flow across the entire volume of the sample. The ac excitation magnetic field in the primary is shown in blue while the field induced in the pickup coils through the currents induced in the sample is shown in red. A schematic plot of the induced current profile across the sample cross section at different f is shown. (b) Shows at a higher frequency the nature of the induced current distribution, which flows only in the TI's high conducting surface states. The nature of the excitation field in the excitation coil (blue) and the induced field in the pickup coil (red) are also shown. (c) Shows the pickup voltage response with sample surface area at 5 kHz, 160 K and 65 kHz, 25 K.

frequency and higher T is related to the bulk contribution to conductivity, where $V(T)$ shows a thermally activated behavior.

At low T, our transport measurements in Fig. 1 as well as past observations [13,14,21,22] have confirmed the dominance of surface contribution to conductivity at low T in the TI. In this low T regime, our pickup signal exhibits a linear frequency-dependent regime. This suggests that the linear frequency dependence of the pickup signal is related to the surface conducting state in the TI. Similarly, at high T, the observation from our transport measurements and those of other measurements [21,22] of the emergence of bulk conducting response coincide with the observed quadratic dependence at low frequencies of the pickup signal. Therefore, this quadratic frequency-dependence at low frequency of the pickup signifies the emergence of bulk contribution to electrical conductivity. Another possible explanation for the observed frequency dependence is given as follows: The pickup voltage develops due to the current induced in the sample. These induced currents depend on the electrical conductivity of the sample. Based on the above discussion, the electrical conductivity of the TI has two contributions, $\sigma_b(T) = \sigma_{b0}\exp(-(\Delta/K_bT))$ and $\sigma_s(T) = 1/(C+DT)$. The pickup voltage is given by (see S9 within the Supplemental Material [46] for detailed calculation)

$$V_{\text{pickup}}(\omega) = \xi(r,z)\Phi\omega^2 e^{-i\omega t}\left[\frac{\sigma_{os}}{C+DT} + \frac{\sigma_{ob}}{e^{\Delta/KT}}\right]\frac{1}{1+i\omega\tau},$$

(1)

where $\xi(r,z)$ is a geometric factor, which is a function of the pickup coil radius (r) and the height between the two coils (z), Φ is the magnetic flux passing through the sample, τ is scattering time scale, and $\omega = 2\pi f$. Terahertz spectroscopy measurements [49,50] show that the bulk and surface have different values of scattering time scale τ. Hence, we assume two different limits in Eq. (1) (see S9 within the Supplemental Material [46] for details). When the bulk state dominates in conduction, we use a limit $f\tau \ll 1$. Under this assumption, Eq. (1) gives us

$$V_{\text{pickup}}(f) \approx \Phi_0\xi(r,z)f^2 e^{-i2\pi ft}\sigma_b.$$

(2)

If the surface state starts to dominate in conduction, using the limit $f\tau \gg 1$, Eq. (1) shows $V(f) \propto f^\alpha$, viz.,

$$V_{\text{pickup}}(f) \approx \Phi_0\xi(r,z)e^{-i2\pi ft}\sigma_s f.$$

(3)

Figure 5(a) shows the $V(T)$ measurements of Fig. 3(b) for the $S69$ sample. The data is fitted with the expression

$$V(T) = P_{\text{surface}}[\text{Eq.}(3)] + P_{\text{bulk}}[\text{Eq.}(2)],$$

(4)

where P_{surface} and P_{bulk} are mean fractions of the surface and bulk contributions to the pickup voltage with
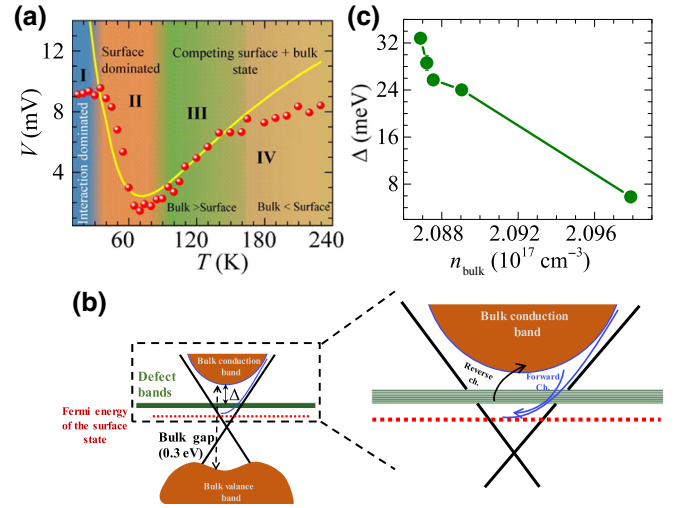

FIG. 5. (a) The $V(T)$ response for sample $S69$ is shown in red circles for 65 kHz frequency. The solid yellow line is the fit to the data done using Eq. (4). Four distinct regions (I–IV) are shown with four different colors (see text for details). (b) A schematic showing the bulk conduction and valence bands as well as the surface states. The schematic on the right is an expanded portion of the left schematic. The violet curve in the right schematic shows upward band bending of the conducting band toward the Fermi energy of the surface state due to Se vacancies. The forward channel (Forward Ch.) is associated with electrons migrating from the bulk to the surface, the reverse channel (Reverse Ch.) is associated with electrons being thermally activated from the surface into the bulk. Black lines show the Dirac cone associated with the surface states. The Fermi energy is shown by the red dotted line. The green region represents the defect states produced by the Se vacancies. The activation energy gap (Δ) is between the defect state and minima of the conduction band. (c) Activation energy gap (Δ) calculated from our model is plotted as a function of bulk carrier (n_{bulk}). The n_{bulk} is calculated using $n_{\text{bulk}} = \sigma_b/\mu(d)e$, where $\mu(d) = 3000/[1+(140/d)]$ [23] is the thickness (d) dependent mobility and $\sigma_b \sim 10^3$ S/m (based on the value used in the simulations above).

$P_{\text{surface}} + P_{\text{bulk}} = 1$. Note the T dependence of σ_s and σ_b has already been shown by the black line and red dashed line in Fig. 3(b), respectively. The $S69$ data in Fig. 5(a) fits with $P_{\text{surface}} = 35\%$, $P_{\text{bulk}} = 65\%$. Note that at 65 kHz, the P_{surface} is sensitive to the thin conducting regions within the sample where shielding currents are induced by the ac field. The minima in $V(T)$ at 70 K [Fig. 5(a)] suggests regions in the TI, which exhibit predominantly surface conductivity responses at low T [Fig. 3(c)], with increasing T begin to display bulk conductivity. The surface contribution is gradually degraded by transport channels being created in the bulk. As a result, we see only an average 35% contribution to the total conductivity from the surface.

The fitting in Fig. 5(a) shows that at high T above 170 K, there is a deviation from the Eq. (4) fit and the $V(T)$ becomes weakly temperature dependent. We have found in

all the samples, the $V(f)$ at high temperatures exhibits linear and quadratic frequency dependence at high and low frequencies, respectively [eg., see 150 K data in Fig. 3(a)]. This behavior suggests the presence of surface conductivity coexisting with a bulk conducting regime in the sample even at high temperatures. The temperature dependence of $V(T)$ below 70 K in Figs. 3(b) and 5(a) suggests that the electrical conductivity of the sample obeys $\sigma_s(T) = 1/(C + DT)$. This form of temperature dependence of the electrical conductivity has been reported for the surface conducting state in TI [21,22]. The T-dependent part of the electrical conductivity, $\sigma(T) = 1/(C + DT)$, sets in above 40 K (i.e., $D \gg C$). Ours and other investigations [51,52] show the presence of a temperature-independent conductivity regime below 40 K, which is a feature of metallic conductivity of the topologically protected surface states in TI materials. Earlier studies in Bi_2Se_3 studies show that the T dependent conductivity above 40 K is due to electron-phonon interactions [51]. With a lowering of T (below 40 K) where the surface conductivity of the TI dominates, the electron–phonon coupling significantly weakens [12]. From the above expression, the T independent conductivity regime is obtained when $D \ll C$ at $T < 40$. In this temperature regime where conductivity is via the topological surface states, magnetotransport studies show weak antilocalization due to the chiral nature of the currents [21,33,53]. In this regime, studies suggest [33] electron interactions play a role in determining the behavior of the conductivity of the TI materials. Hence, below 40 K where there is a saturated behavior of conductivity, the effect of electron–phonon interaction may be relatively diminished compared to that of electron interaction effects. In view of this, we identify an electron interaction-dominated regime at low T.

Based on our above discussions, in Fig. 5(a), we identify four different regimes: (i) Region I (below approximately 40 K is the strong interaction-dominated surface regime): In this regime, surface conductivity dominates in the TI and conductivity is nearly temperature-independent due to strong electron-electron interaction effects. (ii) Region II (temperature-dependent surface state): Here, the surface state dominates the conductivity of the TI with a temperature dependence of the form $\sigma_s(T) = 1/(C + DT)$ due to the onset of electron-phonon scattering. As the temperature increases, the surface conductivity falls until it reaches close to the bulk conductivity value, which is close to the minima in $V(T)$. (iii) Region III (bulk-dominated state): In this region, which extends from about 70 K to 170 K, Fig. 3(b) shows a good fit to bulk behavior [see dashed red curve in Fig. 3(b)]. However, the fit does not imply that in region III the surface contribution to conductivity is zero. Figure 3(b) shows that in regime III, the surface contribution to conductivity (solid black line) is much smaller than the bulk contribution, due to which the fit to bulk appears to be good and bulk dominates. Figure 3(a) shows that

for temperatures in regime III (such as 90 K and 150 K) the $V(f)$ has a quadratic as well a nearly linear regime $(V(f) \propto f^{\alpha}$, where $\alpha \sim 1)$, which shows the presence of both bulk and surface contributions to conductivity. Hence, region III is a regime with the bulk contribution to conductivity dominating over a weak surface contribution. Here, the response from the bulk in the TI shows a thermally activated conductivity behavior. The typical thermal activation energy scale is estimated to be approximately 6–30 meV by studying five different samples. (iv) Region IV: This is an unusual regime found at high temperatures, where $V(T)$ deviates from the Eq. (4) fit. In this regime, we recall similar linear $V(f)$ behavior [inset Fig. 3(a)]. Just like the weakly T dependent surface conductivity regime is present at low T, we propose the weakly temperature-independent regime at high T is where the effects of surface conductivity of a TI become important once again. We would like to reiterate here that at surface and bulk, both conductivities contribute to the pickup voltage, as the induced currents are generated in both the surface and bulk of the sample. Regions III and IV [Fig. 5(a)] are associated with a competition between bulk and surface state contributions to conductivity. The change in curvature of the $V(T)$ curve in Fig. 5(a) is going from region III to region IV, which signifies a competition between surface and bulk contributions to conductivity. In region III, we have shown that the thermally activated nature of bulk conductivity dominates. Recall the inset of Fig. 3(a) at high T, which shows a nearly linear frequency dependence [viz., $V(f) \propto f^{\alpha}$], where $\alpha \sim 1$ when T is in region IV. This suggests the re-emergence of significant surface contributions to conductivity along with bulk. Here, within temperature window III, the bulk contribution to conductivity dominates over the surface contribution, while in region IV, it is vice versa.

VI. SIMULATIONS OF THE MUTUAL INDUCTANCE MEASUREMENTS

We simulate the electromagnetic response of this topological insulator with defects using COMSOL Multiphysics software. In Fig. 6(a) inset, we first model a defect-free TI with high-conducting thin metallic sheets (yellow) sandwiching a bulk low-conducting slab (blue). We solve the Maxwell equation for the modeled TI subjected to a time varying magnetic field applied using coil parameters identical to those in our experiment (see S2 within the Supplemental Material [46]). We use an ac excitation current of $I = 150$ mA (similar to our experiment). First, the rate of change of the induced flux ($\dot{\varphi} = M\dot{I}$) in the pickup coil is calculated from which the mutual inductance (real and imaginary components) M' and M'' are calculated (analog to our experiments, $M'' \ll M'$). The modeled TI has a crystal thickness and surface area similar to the $S20$ sample, with a thickness of 5 nm for the
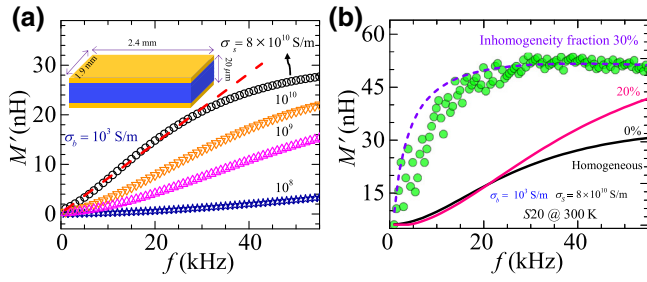
FIG. 6. Inset (a) shows the schematic of an ideal TI. Blue color represents the bulk state and yellow color represents the high conducting surface state. The thickness of the high conducting surface state is taken as 5 nm (thickness of the yellow region), the other relevant dimensions are height = 20 μm, width = 1.9 mm, and length = 2.4 mm. The main panel shows the behavior of the simulated $M'(f)$ for different conductivities of the surface state while keeping the bulk conductivity constant (approximately 10^3 S/m). Red dash line shows the linear dependence of M'. It is clear that M' seems to saturate beyond 40 kHz whereas the experimentally measured data shows saturation from 20 kHz onward. (b) Shows the M' is simulated as a function of f for different inhomogeneity levels (0%, 20%, and 30%) by incorporating conducting channels inside the bulk (see text for details and S2 within the Supplemental Material [46]). Comparison of simulation and experimental results (scattered data) of M' is shown for $S20$ sample at room temperature.

metallic high-conducting sheets and 20 μm for the bulk insulating layer. The above is based on estimates indicating the thickness of the conducting surface in Bi$_2$Se$_3$ is between 5 to 10 nm [54,55]. In Fig. 6(a), we see the data begins to look like the experimental $V(f)$ data when the bulk conductivity $\sigma_b \sim 10^3$ S/m and the conductivity of the metallic sheets $\sigma_s \sim 10^{11}$ S/m (note OFHC triple nine purity copper has a conductivity approximately 10^8 S/m). Earlier transport measurements have shown conductivity of the surface states in Bi$_2$Se$_3$ of approximately 10^4 to 10^5 S/m [22,56]. It may be mentioned here that in conventional transport measurements due to an inability to distinguish between bulk and surface conducting channels, the measured surface conductivity via transport measurements could be much lower than the actual value. (Details on the behavior of the skin depth and its estimate are shown in S10 within the Supplemental Material [46].) Note that the relation between M' and the induced voltage in the pickup coil is $V' \propto \omega M'$ (as $M'' \ll M'$ or $V'' \ll V'$, $M'(f) = {}^{V'(f)}/_{\omega I}$ where $I = 150$ mA, $\omega = 2\pi f$). Figure 6(a) shows simulated M' as a function of frequency for different conductivities of the TI surface while keeping the bulk conductivity constant at approximately 10^3 S/m. The value σ_b we use is based on estimates in literature [35]. The general behavior of $M'(f)$ is that it increases linearly with frequency and it saturates at higher frequencies. At the lower frequency regime where $M'(f) \propto f$ [see dotted line drawn in Fig. 6(a)], it corresponds to the pickup voltage,

$V(f) \propto f^2$. At higher f where the M' is weakly dependent on f, it corresponds to $V(f) \propto f$. Figure 6(a) shows that the M' begins to show saturating features as the surface state conductivity (σ_s) increases. This confirms that highly conducting surface states are responsible for the nearly linear frequency dependence of pickup voltage $V(f)$ in the high-frequency regime [see Fig. 3]. Note that while the simulations in Fig. 6(a) show the $M'(f)$ saturates above 40 kHz, our experiments, Fig. 3 shows that $V(f) \propto f^\alpha$ (where $\alpha \sim 1$) regime (i.e., $M'(f) \sim$ constant) sets in above 20 kHz and not from 40 kHz.

In order to match our simulations with the observed saturation of $M'(f)$ at relatively lower f (from 20 kHz), without significantly enhancing the surface conductivity σ_s (far beyond what has been reported in literature for these samples), we consider a situation where conducting channels exist in the bulk, which connect to the high-conducting surface states. We argue later that these high-conducting channels in the bulk are generated by Se vacancies. Such a state of the TI we refer to as an inhomogeneous topological insulator state. We incorporate inhomogeneity in our model for the TI by considering a distribution of solid high-conductivity cylindrical regions threading through the bulk of the sample connecting the top and bottom high-conducting surface sheets of the TI (see S2 within the Supplemental Material [46] for a schematic of the modeled inhomogeneous TI system). In our simulation, the percentage inhomogeneity in the TI is varied by changing the density of cylinders and the conductivity of the cylinders is taken as σ_s. Figure 6(b) shows that the results of simulations match with our experimental results by using $\sigma_s \sim 10^{11}$ S/m, $\sigma_b \sim 10^3$ S/m, and 30% inhomogeneity. The introduction of the 30% inhomogeneity in our TI model causes the $M'(f)$ to saturate from lower frequencies of 20 kHz. The presence of 30% inhomogeneity in the sample would affect the net bulk electrical conductivity. However, estimating the extent of change in the net bulk electrical conductivity is not clear as yet as this would statistically depend on the fraction of high conductivity and low channels contributing to the electrical conduction paths when electric current flows through the bulk. We find that our above simulation results are not sensitive to the details of the spatial distribution of inhomogeneity introduced in the TI, but rather the results are quite sensitive to the inhomogeneity fraction in the TI (see S2 within the Supplemental Material [46]). Figure 6(b) shows the close match between the simulated $M'(f)$ (purple dashed line) and the measured voltage data (green scattered data) for the $S20$ sample at 300 K using the inhomogeneous TI model. Since in this high-frequency regime the skin depth in the TI is estimated to be approximately 100 nm (see S10 within the Supplemental Material [46]), we suggest that the inhomogeneities discussed above are clustered over length scales, which are ≤100 nm (in our model, we take the spatial extent of inhomogeneity in the TI as the

diameter of the cylinders). Due to the presence of parallel channels of electrical conduction between the surface and bulk of the TI material, it is difficult to identify the surface conductance and inhomogeneity through the bulk in a transport measurement, especially at intermediate temperature regimes where both contributions are admixed. However, the analysis of SdH oscillations at different T help to give a signature of the onset of the bulk contribution to electrical conductivity.

Analysis of the SdH oscillations in our Bi_2Se_3 (see Fig. 1 and its caption for details) using the LK equation [35,57,58] gives a frequency of the SdH oscillations $(F) = 46.95 \pm 0.25$ T. As $F = (4\pi^2\hbar n_s)/e$, where n_s is the surface carrier density, we get $n_s = (2.268 \pm 0.012)$ cm^{-2}, which compares well with earlier estimates in this batch of samples [35]. Using n_s we estimate the Fermi wave vector for the two-dimensional (2D) surface states in our sample is $k_f = \sqrt{2\pi n_s} = (0.0377 \pm 0.0027)$ Å^{-1}. By comparing this k_F value with the ARPES spectrum measured for Bi_2Se_3 samples (see Fig. 1 of Ref. [59]), we see that the Fermi energy (E_f) should be located approximately 30 meV above the Dirac point and about 100 meV below the bottom of the bulk conduction band (this comparison is illustrated in S12 within the Supplemental Material [46]). If we assume the origin of the SdH oscillation in the transport measurements is due to the bulk electrons, then bulk carrier density should be $k_F^2/4\pi c = 3.8 \times 10^{18}$ cm^{-3}, where $c = 28.64$ Å is the Bi_2Se_3 lattice spacing along the c axis. However, the bulk carrier density (n_{bulk}) in the TI material as estimated from the Hall coefficient [Fig. 1(b)] is 2.83×10^{19} cm^{-3}. This comparison shows that the features of our transport data at low T cannot be reconciled with bulk conduction electrons contributing to conductivity, rather they are arising from 2D surface electrons. The SdH oscillations in the transport measurements (see Fig. 1) analyzed using the LK equation also reveal information on the Berry phase, $\phi = 2\pi\beta$ [see Fig. 1(b) inset]. For the 2D, the Dirac fermion in TI $\phi = \pi$ suppresses the back scattering from disorder due to destructive interference. From the analysis of the SdH at different T, we obtain a value close to π at low T below 10 K [see Fig. 1(b) inset]. Thus, at low T, the observed value of ϕ close to π suggests that the SdH oscillation arises from 2D surface Dirac electrons. As bulk contributions to conductivity increase with T, the SdH oscillations weaken and disappear [see Fig. 1(a)] and the ϕ value significantly deviates from π above 10 K [see Fig. 1(b) inset]. Therefore, at low T, the transport data shows conductivity of the TI is surface-dominated, which gets progressively affected as the bulk conductivity sets in at higher T. However, the temperature range over which the above analysis can be done is very limited. While the above observations are consistent with our results based on pickup coil measurements, our technique is applicable over a wider T range.

VII. DISCUSSION ON THE ROLE OF DISORDER IN Bi_2Se_3

A bulk gap in Bi_2Se_3 of 0.3 eV suggests that thermally activated conductivity should be seen at significantly elevated temperatures, but we see activated conductivity from $T \sim 70$ K onward [viz., the region III in Fig. 5(a)]. In Bi_2Se_3 samples, it is known Se vacancies add defect states in the bulk. These defects states add excess electrons in the bulk due to which the conductivity of the bulk increases. The measured Δ values are almost an order of magnitude smaller than the estimates of the bulk band gap in Bi_2Se_3 of about 0.3 eV [7,10,26,27]. One possible scenario could be that the gap Δ corresponds to a gap between the defect states generated by Se vacancies and the bottom of the conduction band [see Fig. 5(b)]. It is known that Se vacancies causes an upward band bending [Fig. 5(b)] of the states near the bottom of the conduction band toward the surface state [60]. The band bending favors the migration of electrons generated in the bulk (due to Se vacancies) to the surface. We refer to this as the forward channel [see Fig. 5(b)]. Above 70 K, the thermal energy is sufficient for thermal activation of charges from defect states into the bulk. We refer to this as the reverse channel. This reverse channel for charge migration begins at $T > \Delta/k_B$ [Fig. 5(b)]. Recall that in Bi_2Se_3, excess charge carriers are produced by Se vacancies. In Fig. 5(c), we estimate the behavior of carrier density in the bulk (n_{bulk}) using a known form [23], $n_{bulk} = \sigma_b/\mu(d)e$, where $\mu(d) = {}^{3000}/_{[1+(140/d)]}$ is the thickness (d) dependent mobility and $\sigma_b \sim 10^3$ S/m. Thus, the activation barrier Δ is larger for smaller bulk carrier densities. Akin to a tight bindinglike picture, we propose the hopping back and forth of charges between the defect states in the bulk and surface states enhances the average kinetic energy of charges, leading to the formation of a broad defect band and this also helps to open a gap Δ near the surface states. The Δ decreases with n_{bulk} as seen in Fig. 5(c), which could be a result of enhanced Coulombic interactions in these lower electron-doped samples suppressing the kinetic energy and localizing the charges. Enhanced interaction effects lead to the weak T dependence of conductivity not only at low T below 40 K, but also at high T above 180 K [Fig. 5(a)]. Thus, selenium vacancy-induced electron doping of the bulk leads to an interplay between bulk and surface conductivities, leading to an inhomogeneous TI state in Bi_2Se_3. Based on the above discussion, we propose that in region III of Fig. 5(a), the bulk contribution to the conductivity dominates over that of the surface due to thermal excitation of charge carrier in the bulk state. However, at higher temperatures (region IV), the excess charge migration to the surface state due to Se vacancies results in the contribution of the surface conductivity to enhance it once again. It is due to this effect where we see the experimental data deviating from the fitting line in the high-temperature regime

[region IV in Fig. 5(a)]. We believe more detailed work using techniques such as STM and ARPES is required to probe the effect of defect states lying within the bulk and the resulting gap emerging in the TI.

VIII. CONCLUSIONS

In conclusion, our noncontact two-coil mutual-inductance measurements in Bi_2Se_3 single crystals suggest that the surface states are coupled to the bulk state with filamentary high-conducting structures. The inhomogeneous state gets precipitated in the bulk of the TI only above the threshold temperature, which is associated with the activation of charge between the surface and bulk. This leads to an interplay between bulk- and surface-dominated transport regimes at different T, which is produced as a result of disorder introduced in the system. While material disorder leads to interplay between bulk and surface conductivities in a TI material, it is also responsible for resurfacing of the surface conductivity at high temperature, which is a potentially useful feature for applications.

[1] Joel E. Moore, The birth of topological insulators, Nature **464,** 194 (2010).

[2] M. Z. Hasan and C. L. Kane, Colloquium: Topological insulators, Rev. Mod. Phys. **82,** 3045 (2010).

[3] D. Hsieh, D. Qian, L. Wray, Y. Xia, Y. S. Hor, R. J. Cava, and M. Z. Hasan, A topological Dirac insulator in a quantum spin Hall phase, Nature **452,** 970 (2008).

[4] L. Fu, C. L. Kane, and E. J. Mele, Topological Insulators in Three Dimensions, Phys. Rev. Lett. **98,** 106803 (2007).

[5] D. Hsieh, Y. Xia, L. Wray, D. Qian, A. Pal, J. H. Dil, J. Osterwalder, F. Meier, G. Bihlmayer, C. L. Kane, Y. S. Hor, R. J. Cava, and M. Z. Hasan, Observation of unconventional quantum spin textures in topological insulators, Science **323,** 919 (2009).

[6] Lukas Zhao, Haiming Deng, Inna Korzhovska, Zhiyi Chen, Marcin Konczykowski, Andrzej Hruban, Vadim Oganesyan, and Lia Krusin-Elbaum, Singular robust room-temperature spin response from topological Dirac fermions, Nat. Mater. **13,** 580 (2014).

[7] Y. Xia, D. Qian, D. Hsieh, L. Wray, A. Pal, H. Lin, A. Bansil, D. Grauer, Y. S. Hor, R. J. Cava, and M. Z. Hasan, Observation of a large-gap topological-insulator class with a single Dirac cone on the surface, Nat. Phys. **5,** 398 (2009).

[8] Y. L. Chen, J. G. Analytis, J.-H. Chu, Z. K. Liu, S.-K. Mo, X. L. Qi, H. J. Zhang, D. H. Lu, X. Dai, Z. Fang, S. C. Zhang, I. R. Fisher, Z. Hussain and Z.-X. Shen, Experimental realization of a three-dimensional topological insulator Bi_2Te_3, Science **325,** 178–181 (2009).

[9] Peng Cheng, *et al.*, Landau quantization of topological surface states in Bi_2Se_3, Phys. Rev. Lett. **105,** 076801 (2010).

[10] H. Zhang, C. X. Liu, X. L. Qi, X. Dai, Z. Fang, and S. C. Zhang, Topological insulators in Bi_2Se_3, Bi_2Te_3 and Sb_2Te_3 with a single Dirac cone on the surface, Nat. Phys. **5,** 438 (2009).

[11] Zhuojin Xie, *et al.*, Orbital-selective spin texture and its manipulation in a topological insulator, Nat. Commun. **5,** 3382 (2014).

[12] Z.-H. Pan, A. V. Fedorov, D. Gardner, Y. S. Lee, S. Chu, and T. Valla, Measurement of an Exceptionally Weak Electron-Phonon Coupling on the Surface of the Topological Insulator Bi_2Se_3 Using Angle-Resolved Photoemission Spectroscopy, Phys. Rev. Lett. **10,** 187001 (2012).

[13] D. X. Qu, Y. S. Hor, J. Xiong, R. J. Cava, and N. P. Ong, Quantum oscillations and hall anomaly of surface states in the topological insulator Bi_2Te_3, Science **329,** 821 (2010).

[14] L. A. Jauregui, M. T. Pettes, L. P. Rokhinson, L. Shi, and Y. P. Chen, Gate tunable relativistic mass and berry's phase in topological insulator nanoribbon field effect devices, Sci. Rep. **5,** 8452 (2015).

[15] Pedram Roushan, Jungpil Seo, Colin V. Parker, Y. S. Hor, D. Hsieh, Dong Qian, Anthony Richardella, M. Z. Hasan, R. J. Cava, and Ali Yazdani, Topological surface states protected from backscattering by chiral spin texture, Nature **460,** 1106 (2009).

[16] X. L. Qi and S. C. Zhang, Topological insulators and superconductors, Rev. Mod. Phys. **83,** 1057 (2011).

[17] H. Soifer, A. Gauthier, A. F. Kemper, C. R. Rotundu, S.-L. Yang, H. Xiong, D. Lu, M. Hashimoto, P. S. Kirchmann, J. A. Sobota, and Z.-X. Shen, Band-Resolved Imaging of Photocurrent in a Topological Insulator, Phys. Rev. Lett. **122,** 167401 (2019).

[18] S. A. Wolf, D. D. Awschalom, R. A. Buhrman, J. M. Daughton, S. von Molnár, M. L. Roukes, A. Y. Chtchelkanova, and D. M. Treger, Spintronics: a spin-based electronics vision for the future, Science **294,** 1488 (2001).

[19] D. K. Kim, Y. Lai, B. Diroll, C. Murray, and C. F. Kagan, Flexible and low-voltage integrated circuits constructed from high-performance nanocrystal transistors, Nat. Commun. **3,** 1216 (2012).

[20] P. J. Leek, J. M. Fink, A. Blais, R. Bianchetti, M. Göppl, J. M. Gambetta, D. I. Schuster, L. Frunzio, R. J. Schoelkopf, and A. Wallraff, Observation of Berry's phase in a solid-state qubit, Science **318,** 1889 (2007).

[21] B. F. Gao, P. Gehring, M. Burghard, and K. Kern, Gate-controlled linear magnetoresistance in thin Bi_2Se_3 sheets, Appl. Phys. Lett. **100,** 212402 (2012).

[22] Yang Xu, Ireneusz Miotkowski, Chang Liu, Jifa Tian, Hyoungdo Nam, Nasser Alidoust, Jiuning Hu, Chih-Kang Shih, M. Zahid Hasan, and Yong P. Chen, Observation of topological surface state quantum Hall effect in an intrinsic three-dimensional topological insulator, Nat. Phys. **10,** 956 (2014).

[23] Yong Seung Kim, Matthew Brahlek, Namrata Bansal, Eliav Edrey, Gary A. Kapilevich, Keiko Iida, Makoto Tanimura, Yoichi Horibe, Sang-Wook Cheong, and Seongshik Oh, Thickness-dependent bulk properties and weak antilocalization effect in topological insulator Bi_2Se_3, Phys. Rev. B **84,** 073109 (2011).

[24] Diptasikha Das, K. Malik, S. Bandyopadhyay, D. Das, S. Chatterjee, and A. Banerjee, Magneto-resistive property study of direct and indirect band gap thermoelectric Bi-Sb alloys, Appl. Phys. Lett. **105**, 082105 (2014).

[25] J. G. Analytis, R. D. McDonald, S. C. Riggs, J. H. Chu, and G. S. Boebinger, Two-dimensional surface state in the quantum limit of a topological insulator, Nat. Phys. **6**, 960 (2010).

[26] P. Larson, V. A. Greanya, W. C. Tonjes, R. Liu, S. D. Mahanti, and C. G. Olson, Electronic structure of Bi_2X_3 ($X = S$, Se, T): compounds: Comparison of theoretical calculations with photoemission studies, Phys. Rev. B **65**, 085108 (2001).

[27] I. A. Nechaev, R. C. Hatch, M. Bianchi, D. Guan, C. Friedrich, I. Aguilera, J. L. Mi, B. B. Iversen, S. Blügel, Ph. Hofmann, and E. V. Chulkov, Evidence for a direct band gap in the topological insulator Bi_2Se_3 from theory and experiment, Phys. Rev. B **87**, 121111 (2013).

[28] G. R. Hyde, H. A. Beale, I. L. Spain, and J. A. Woollam, Electronic properties of Bi_2Se_3 crystals, J. Phys. Chem. Solids **35**, 1719 (1974).

[29] H. M. Benia, C. Lin, K. Kern, and C. R. Ast, Reactive Chemical Doping of the Bi_2Se_3 Topological Insulator, Phys. Rev. Lett. **107**, 177602 (2011).

[30] J. M. Zhang, W. Ming, Z. Huang, G. B. Liu, X. Kou, Y. Fan, K. L. Wang, and Y. Yao, Electronic and magnetic properties of the magnetically doped topological insulators Bi_2Se_3 Bi_2Te_3, and Sb_2Te_3, Phys. Rev. B **88**, 235131 (2013).

[31] Nicholas P. Butch, Kevin Kirshenbaum, Paul Syers, Andrei B. Sushkov, Gregory S. Jenkins, H. Dennis Drew, and Johnpierre Paglione, Strong surface scattering in ultrahigh-mobility Bi_2Se_3 topological insulator crystals, Phys. Rev. B **81**, 241301 (2010).

[32] H. D. Li, Z. Y. Wang, X. Kan, X. Guo, H. T. He, Z. Wang, J. N. Wang, T. L. Wong, N. Wang, and M. H. Xie, The van der Waals epitaxy of Bi_2Se_3 on the vicinal Si (111) surface: an approach for preparing high-quality thin films of a topological insulator, New. J. Phys. **12**, 103038 (2010).

[33] Minhao Liu, Cui-Zu Chang, Zuocheng Zhang, Yi Zhang, Wei Ruan, Ke He, Li-li Wang, Xi Chen, Jin-Feng Jia, Shou-Cheng Zhang, Qi-Kun Xue, Xucun Ma, and Yayu Wang, Electron interaction-driven insulating ground state in Bi_2Se_3 topological insulators in the two-dimensional limit, Phys. Rev. B **83**, 165440 (2011).

[34] K. Hoefer, C. Becker, C. D. Rata, J. Swanson, P. Thalmeier, and L. H. Tjeng, Intrinsic conduction through topological surface states of insulating Bi_2Te_3 epitaxial thin films, Proc. Natl Acad. Sci. A**111**, 14979 (2014).

[35] T. R. Devidas, E. P. Amaladass, Shilpam Sharma, R. Rajaraman, D. Sornadurai, N. Subramanian, Awadhesh Mani, C. S. Sundar, and A. Bharathi, Role of Se vacancies on Shubnikov-de Haas oscillations in Bi_2Se_3: A combined magneto-resistance and positron annihilation study, Euro. Phys. Lett. **108**, 67008 (2014).

[36] E. P. Amaladass, T. R. Devidas, S. Sharma, C. S. Sundar, A. Mani, and A. Bharathi, Magneto-transport behaviour of $Bi_2Se_{3-x}Te_x$: role of disorder, J. Phys. Condens. Matter. **28**, 075003 (2016).

[37] C. E. ViolBarbosa, Chandra Shekhar, Binghai Yan, S. Ouardi, Eiji Ikenaga, G. H. Fecher, and C. Felser, Direct observation of band bending in the topological insulator Bi_2Se_3, Phys. Rev. B **88**, 195128 (2013).

[38] Desheng Kong, Judy J. Cha, Keji Lai, Hailin Peng, James G. Analytis, Stefan Meister, Yulin Chen, Hai-Jun Zhang, Ian R. Fisher, Zhi-Xun Shen, and Yi Cui, Rapid surface oxidation as a source of surface degradation factor for Bi_2Se_3, ACS Nano **5**, 4698 (2011).

[39] Mintu Mondal, Anand Kamlapure, Madhavi Chand, Garima Saraswat, Sanjeev Kumar, John Jesudasan, L. Benfatto, Vikram Tripathi, and Pratap Raychaudhuri, Phase Fluctuations in a Strongly Disordered s-Wave NbN Superconductor Close to the Metal-Insulator Transition, Phys. Rev. Lett. **106**, 047001 (2011).

[40] Anand Kamlapure, Mintu Mondal, Madhavi Chand, Archana Mishra, John Jesudasan, Vivas Bagwe, L. Benfatto, Vikram Tripathi, and Pratap Raychaudhuri, Measurement of magnetic penetration depth and superconducting energy gap in very thin epitaxial NbN films, Appl. Phys. Lett **96**, 072509 (2010).

[41] Ming-Chao Duan, Zhi-Long Liu, Jian-Feng Ge, Zhi-Jun Tang, Guan-Yong Wang, Zi-Xin Wang, Dandan Guan, Yao-Yi Li, Dong Qian, Canhua Liu, and Jin-Feng Jia, Development of in situ two-coil mutual inductance technique in a multifunctional scanning tunneling microscope, Rev. Sci. Instrum. **88**, 073902 (2017).

[42] Indranil Roy, Prashant Chauhan, Harkirat Singh, Sanjeev Kumar, John Jesudasan, Pradnya Parab, Rajdeep Sensarma, Sangita Bose, and Pratap Raychaudhuri, Dynamic transition from Mott-like to metal-like state of the vortex lattice in a superconducting film with a periodic array of holes, Phys. Rev. B **95**, 054513 (2017).

[43] J. H. Claassen, M. L. Wilson, J. M. Byers, and S. Adrian, Optimizing the two-coil mutual inductance measurement of the superconducting penetration depth in thin films, J. Appl. Phys. **82**, 6 (1997).

[44] Stefan J. Turneaure, Eric R. Ulm, and Thomas R. Lemberger, Numerical modeling of a two-coil apparatus for measuring the magnetic penetration depth in superconducting films and arrays, J. Appl. Phys. **79**, 4221 (1996).

[45] H. Hochmuth and M. Lorenz, Inductive determination of the critical current density of superconducting thin films without lateral structuring, Physica C **220**, 209 (1994).

[46] See Supplemental Material at http://link.aps.org/supplemental/10.1103/PhysRevApplied.12.014056 for S1 section, which deals with the coil details; S2 section shows the differential equations and geometry of the measurement configuration, which are used to solve the differential equations by the COMSOL software; S3 section shows the background and pure Cu sheet pickup signal; S4, S5, S6, S7 and S8 sections show the *S*20, *S*69, *S*75, *S*51, and *S*82 samples' pickup signals, respectively; S9 section deals with the mathematical calculation of the pickup voltage; S10 section shows the skin depth calculation of Bi_2Se_3; S11 section is the image of the em response of Bi_2Se_3 for lower and higher frequencies; S12 section deals with position of the Fermi level of Bi_2Se_3.

[47] N. Ni, M. E. Tillman, J.-Q. Yan, A. Kracher, S. T. Hannahs, S. L. Bud'ko, and P. C. Canfield, Effects of Co substitution

on thermodynamic and transport properties and anisotropic H_{c2} in $Ba(Fe_{1-x}Co_x)_2As_2$ single crystals, Phys. Rev. B **78,** 214515 (2008).

[48] B. Bag, K. Vinod, A. Bharathi, and S. S. Banerjee, Observation of anomalous admixture of superconducting and magnetic fractions in $BaFe_{2-x}Co_xAs_2$ single crystals, New J. Phys. **18,** 063025 (2016).

[49] Liang Wu, M. Brahlek, R. Valdés Aguilar, A. V. Stier, C. M. Morris, Y. Lubashevsky, L. S. Bilbro, N. Bansal, S. Oh, and N. P. Armitage, A sudden collapse in the transport lifetime across the topological phase transition in $(Bi_{1-x}In_x)_2Se_3$, Nat. Phys. **9,** 410 (2013).

[50] M. Hajlaoui, E. Papalazarou, J. Mauchain, G. Lantz, N. Moisan, D. Boschetto, Z. Jiang, I. Miotkowski, Y. P. Chen, A. Taleb-Ibrahimi, L. Perfetti, and M. Marsi, Ultrafast surface carrier dynamics in the topological insulator Bi_2Te_3, Nano Lett. **12,** 3532 (2012).

[51] Dohun Kim, Qiuzi Li, Paul Syers, Nicholas P. Butch, Johnpierre Paglione, S. Das Sarma, and Michael S. Fuhrer, Intrinsic Electron-Phonon Resistivity of Bi_2Se_3 in the Topological Regime, Phys. Rev. Lett. **109,** 166801 (2012).

[52] Zhi Ren, A. A. Taskin, Satoshi Sasaki, Kouji Segawa, and Yoichi Ando, Large bulk resistivity and surface quantum oscillations in the topological insulator Bi_2Te_2Se, Phys. Rev. B **82,** 241306(R) (2010).

[53] Wen Jie Wang, Kuang Hong Gao, and Zhi Qing Li, Thickness-dependent transport channels in topological insulator Bi_2Se_3 thin films grown by magnetron sputtering, Sci. Rep. **6,** 25291 (2016).

[54] Matthew Brahlek, Nikesh Koirala, Maryam Salehi, Namrata Bansal, and Seongshik Oh, Emergence of Decoupled Surface Transport Channels in Bulk Insulating Bi_2Se_3 Thin Films, Phys. Rev. Lett. **113,** 026801 (2014).

[55] G. L. Sun, L. L. Li, X. Y. Qin, D. Li, T. H. Zou, H. X. Xin, B. J. Ren, J. Zhang, Y. Y. Li, and X. J. Li, Enhanced thermoelectric performance of nanostructured topological insulator Bi_2Se_3, Appl. Phys. Lett. **106,** 053102 (2015).

[56] Yoichi Ando, Topological insulator materials, J. Phys. Soc. Jpn. **82,** 102001 (2013).

[57] D. Schoenberg, *Magnetic Oscillations in Metals* (Cambridge University Press, London, 1984), p. 66.

[58] Kazuma Eto, Zhi Ren, A. A. Taskin, Kouji Segawa, and Yoichi Ando, Angular-dependent oscillations of the magnetoresistance in Bi_2Se_3 due to the three-dimensional bulk Fermi surface, Phys. Rev. B **81,** 195309 (2010).

[59] Marco Bianchi, Dandan Guan, Shining Bao, Jianli Mi, Bo Brummerstedt Iversen, Philip D.C. King, and Philip Hofmann, Coexistence of the topological state and a two-dimensional electron gas on the surface of Bi_2Se_3, Nat. Comm. **1,** 128 (2010).

[60] Matthew Brahlek, Nikesh Koirala, Namrata Bansal, and Seongshik Oh, Transport properties of topological insulators: Band bending, bulk metal-to-insulator transition, and weak anti-localization, Solid State Commun. **215–216,** 54 (2015).